AGU ADVANCING EARTH AND SPACE SCIENCES

Geophysical Research Letters®

Key Points:

- Global-scale estimation of atmospheric instability from synthetic aperture radar high-resolution ocean-roughness observations
- First-order roughness statistics enable estimation on a climatological scale
- O(1 km) roughness characteristics enable estimation on a scene-by-scene basis

Correspondence to:

B. Chapron,
Bertrand.Chapron@ifremer.fr

Obukhov Length Estimation From Spaceborne Radars

Owen O'Driscoll[1], Alexis Mouche[1] , Bertrand Chapron[1] , Marcel Kleinherenbrink[2] , and Paco López-Dekker[2]

[1]University Brest, CNRS, Ifremer, IRD, Laboratoire d'Océanographie Physique et Spatiale (LOPS), IUEM, Plouzané, France, [2]Geoscience and Remote Sensing, Civil Engineering and Geosciences, Delft University of Technology, Delft, The Netherlands

Abstract Two air-sea interaction quantification methods are employed on synthetic aperture radar (SAR) scenes containing atmospheric-turbulence signatures. Quantification performance is assessed on Obukhov length L, an atmospheric surface-layer stability metric. The first method correlates spectral energy at specific turbulence-spectrum wavelengths directly to L. Improved results are obtained from the second method, which relies on a machine-learning algorithm trained on a wider array of SAR-derived parameters. When applied on scenes containing convective signatures, the second method is able to predict approximately 80% of observed variance with respect to validation. Estimated wind speed provides the bulk of predictive power while parameters related to the kilometer-scale distribution of spectral energy contribute to a significant reduction in prediction errors, enabling the methodology to be applied on a scene-by-scene basis. Differences between these physically based estimates and parameterized numerical models may guide the latter's improvement.

Plain Language Summary Global high-resolution satellite observations from the radar-carrying Sentinel-1 constellation are used to estimate ocean-atmosphere stability conditions over the oceans. These observations don't measure the atmospheric state directly. Rather, they capture the kilometer-scale variability of the ocean-surface roughness which is correlated to specific ocean-atmosphere stability conditions. By combining parameters and statistics extracted from the radar measurements with machine learning, estimation performance largely exceeds that of a previously suggested approach. With these results, the disequilibrium between the air and sea surface temperature, central to determining sensible heat fluxes over the oceans, shall be more quantitatively and systematically assessed. These results have the potential of guiding improvements in climate models as differences between our physically based estimates and parameterized climate models may indicate and diagnose shortcomings in the latter.

1. Introduction

Oceans regulate our climate system, with ocean warming accounting for over 90% of the Earth's energy inventory increase between 1971 and 2010 (IPCC, 2013). Fluxes across the air-sea interface are driven by kilometer-scale coupled processes. Temperature variations and gradients at the interface can change near-surface stratification properties. Resulting air-sea fluxes of momentum, heat and water vapor are also affected. On the atmospheric side of this interface, these near-surface stratification properties are generally traced by the occurrence of organized large coherent structures.

Indeed, for decades it has been known that wind fields contain atmospheric stability information within their kilometer-scale organization (e.g., Figure 12 in Grossman, 1982). Vertical temperature and wind gradients lead to microscale convection, $\mathcal{O}(10^2 - 10^3 \text{ m})$, whereas large-scale horizontal gradients result in mesoscale convection, $\mathcal{O}(10^3 - 10^5 \text{ m})$, (Fiedler & Panofsky, 1970; Lilly, 1989). Today, global climate models parameterize the kilometer-scale convection. Future models with the capacity to fully capture all scales of convection up to a climatological level are still decades away (e.g., National Academies of Sciences, Engineering, and Medicine, 2019; Rio et al., 2019). To aid the representation of kilometer-scale marine atmospheric boundary layer (MABL) properties—necessary to project the impact of changing coupled air-sea interactions on a climatological scale (Christensen & Zanna, 2022; Cronin et al., 2019)—more observational quantitative estimates are necessary. Yet, over the oceans, direct insight into the small-scale boundary-layer processes remains rather difficult. Field campaigns (e.g., Bony et al., 2017) are conducted locally with high costs, and optical satellite images are often limited due to low-resolution and high cloud coverage. Synthetic aperture radar (SAR) satellite observations have been proposed as a solution to resolve this data gap (T. D. Sikora & Ufermann, 2004). SAR measurements
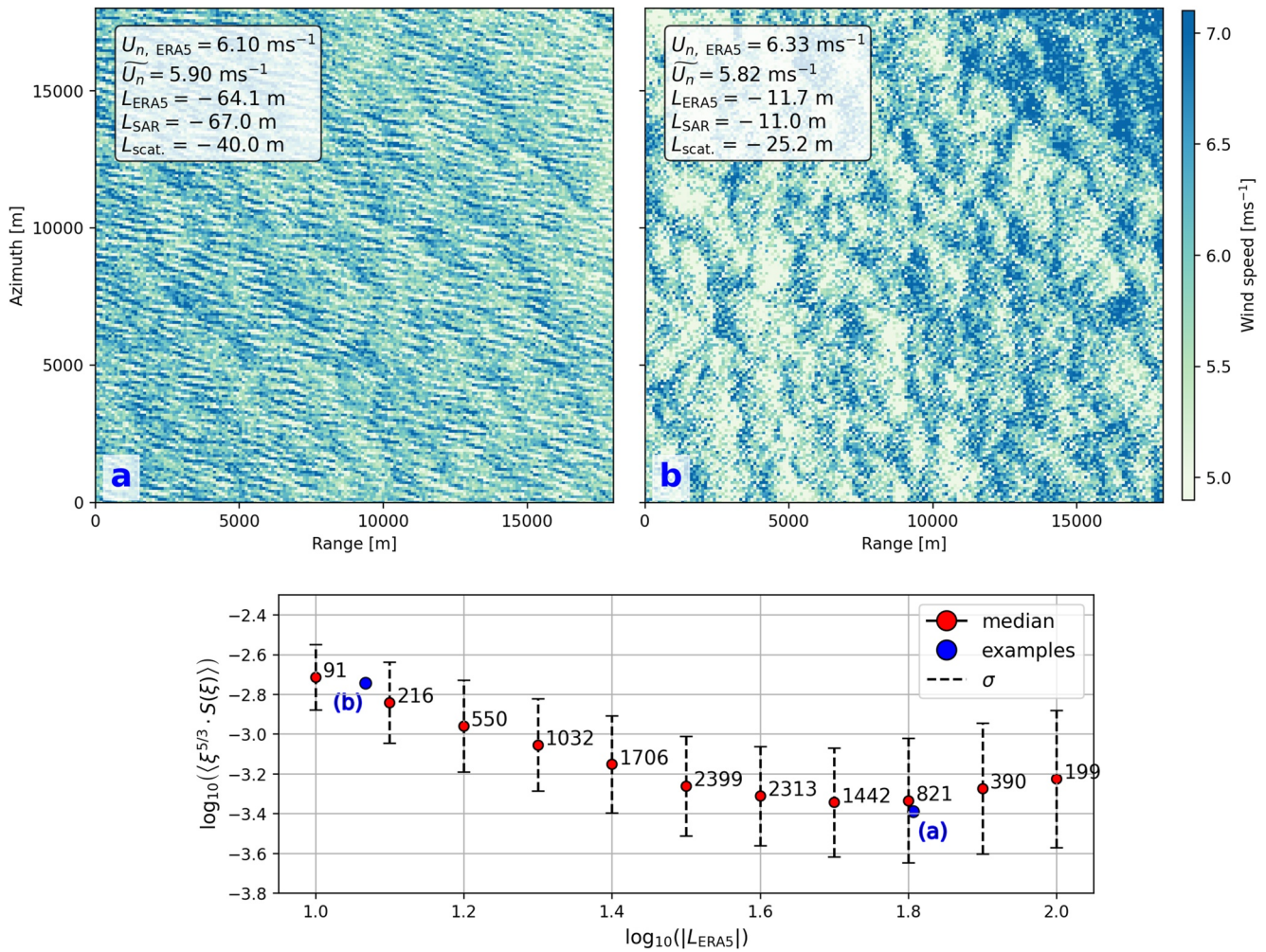
Figure 1. Two wind fields (upper panels) calculated from Sentinel-1B, date: 06-04-2020, absolute orbit: 021017, vignette: 70, product unique ID: BD8A (left) and Sentinel-1A, date: 09-03-2021, absolute orbit: 036917, vignette: 128, product unique ID: 5608 (right), (Lower panel) Atmospheric instability from ERA5 (only unstable conditions considered) versus mean normalized spectral amplitude within the estimated inertial subrange for a specified number of synthetic aperture radar scenes classified as wind streaks or micro convective cells obtained from the same incidence angle (WV2) and similar wind speeds ($U_{n, \text{ERA5}}$ [5.5, 6.5] ms^{-1}). Location on the graph highlighted for the upper left (a) and upper right (b) wind fields.

can indeed capture and quantify sea-surface roughness changes induced by the MABL-stratification properties (Alpers & Brümmer, 1994; T. Sikora et al., 1995; Vandemark et al., 2001). The visibility of MABL-related coherent structures on SAR images is quite systematic as perturbations of surface winds at kilometer-scales, which modulate the centimeter-scale ocean roughness, leave measurable imprints (Wang et al., 2020; Wang, Mouche, Tandeo, et al., 2019; Wang, Tandeo, et al., 2019).

At medium scales, $\mathcal{O}(10 \text{ km})$, first-order wind-field statistics can quantify momentum fluxes, but are generally insufficient at distinguishing between atmospheric regimes. This is illustrated by the upper two SAR-derived wind fields presented in Figure 1d. Despite similar median wind characteristics, corresponding wind-field textures suggest different atmospheric surface-layer stability regimes. This stability is quantified following surface-layer similarity theory from Monin and Obukhov (1954) in

$$L = -\frac{\overline{T}_v u_*^3}{\kappa g \overline{w'T_v'}}, \tag{1}$$

where friction velocity u_*^3 captures the wind-stress related shear production of turbulence and $\overline{w'T_v'}$ the heat-flux related convective production (Stull, 1988). T_v is the virtual temperature, κ the Karman constant and g the

gravitational acceleration. The resulting Obukhov length L could therefore be seen as the balance between two competing sources of turbulence. For greater wind speeds, the shear component generally dominates, forming roll-like wind-field structures. At low wind speeds the convective component dominates, and cell-like structures are formed. Therefore cell- and roll-like structures span different, though partially overlapping, parts of the wind-speed range. Obukhov length is proportional to atmospheric stability parameter ζ following

$$\zeta = \frac{z}{L} \qquad (2)$$

with z being the measurement height. A negative ζ-sign represents unstable conditions. This study works with a constant measurement height of 10 m such that the inverse of L gives consistent insight into atmospheric stability.

Co-located reanalysis data from the European Centre for Medium-Range Weather Forecasts' (ECMWF) ERA5 confirms that L corresponding to the second wind field, whose cell-like texture contrasts the streaky patterns of the former (ignoring the swell), indicates greater instability. SAR measurements are thus apparently capable of capturing high-resolution, $\mathcal{O}(10^1 - 10^3 \text{ m})$, surface wind-field perturbations, which contain information on the local stability conditions.

Young et al. (2000) first proposed to estimate atmospheric surface-layer stability from SAR imagery by relying on work from J. C. Kaimal et al. (1972) and J. Kaimal et al. (1976), and assuming that the wind-field's spectral amplitude within the microscale inertial subrange is related to atmospheric turbulence. Though this analysis yielded promising results on a handful of case studies (e.g., T. D. Sikora et al., 2000; T. D. Sikora & Thompson, 2002), when applied on a greater collection of SAR scenes its flaws become apparent. The lower graph in Figure 1 indicates that the wind-field spectral amplitude obtained from SAR scenes (y-axis) does not uniquely correspond to an atmospheric stability (x-axis) for convective scenes observed with similar wind speeds and viewing geometries (i.e., similar backscatter amplitudes); spectral amplitudes contain too little information to discriminate between atmospheric stability properties. Furthermore, Young's approach requires a clear spectral peak and inertial subrange within the microscale, a range often obscured in SAR-derived spectra due to the presence of long-wavelength swell (an inevitable consequence of global analyses) or imaging artifacts. Additionally, the selection of constants in Young's approach implicitly assume a specific (currentless) sea state and atmosphere (e.g., $a = 0.011$ and $\Psi = 0.6$ in Equations 3 and 11 of Young et al. (2000) respectively). A clear microscale and adherence to specific sea- and/or atmospheric states cannot be guaranteed for global analyses.

To overcome these uncertainties, a greater quantity of kilometer-scale wind-field information is thus likely necessary. In this study, several additional parameters are derived to improve the characterization of the wind-field's distributed variance, in addition to first-order parameters (such as median wind speed) and parameters originally derived in Young's analytical methodology. Machine Learning (ML) is then employed to connect the additional wind-field information to L. The addition of ML is intended to make up for the lack of an analytical framework through which to combine all derived parameters, to compensate for incorrect assumptions (such as those related to the sea state and atmosphere), to squeeze out extra information on the atmosphere which remained untapped in the purely analytical method and to facilitate the analysis of vast quantities of observations.

Since the launch of ESA's Sentinel-1 missions in 2014 (Sentinel-1A) and 2016 (Sentinel-1B), millions of SAR observations over the oceans have been acquired, capturing a wide variety of air-sea environmental conditions (Wang, Mouche, Foster, et al., 2019). Noteworthy is the SAR-image classification work by Wang, Tandeo, et al. (2019) which provides a means of selecting a subset of convective SAR observations. The aim of this paper is thus to quantify L for convective SAR scenes in a regression sense, rather than in terms of classification (e.g., the ternary stability classification of Stopa et al., 2022). The analysis is first performed on 124,682 SAR scenes, classified as containing convective wind streaks (referred to as rolls throughout this study) to determine to what extent it is possible to further discern between L's within one of Wang et al.'s convective classes. Afterward, the scope is extended by including a similar number of micro convective cells (referred to as cells) to determine the applicability of the approach on a broader range of convective conditions and to assess the importance of kilometer-scale SAR-detected features. Validation is performed by a comparison and regression toward co-located retrievals from ERA5. In Text S1 in Supporting Information S1, the suitability of ERA5 for validation is assessed through a comparison with a smaller, secondary data set comprised of moored buoys.

2. Description of Data

2.1. Observations

C-band SARs onboard the Sentinel-1 constellation are sensitive to surface roughness variations on the centimeter scale (ESA, 2021) and thereby insensitive to most phenomena occurring in the atmosphere. SARs are thus incapable of measuring atmospheric turbulence directly. Instead, SAR quantitatively traces short-scale turbulence-induced roughness patterns on the ocean surface and indirectly approximates the projection of the atmospheric turbulence spectrum. Naturally, roughness patterns may be contaminated by other phenomena which affect the ocean surface such as swell, biological films, rain, etc.

Sentinel-1's C-band radars operate at various exclusive modes with different polarizations. This study uses WaVe mode (WV) observations with a resolution of 5 by 5 m. Measurement and processing artifacts such as smearing, azimuthal cut-off and velocity bunching (e.g., Brüning et al., 1990; Kerbaol et al., 1998; Rizaev et al., 2021) reduce the effective resolution by orders of magnitude. The WV scenes are then resampled to 100 m resolution. All analyzed images are obtained with the radar transmitting and receiving in VV polarization. A total of 249,496 pre-classified WV scenes are selected within the years 2020–2021 which, according to the convolutional neural network from Wang, Tandeo, et al. (2019), contain 124,682 rolls and 124,814 cells. The observations are evenly distributed over both years and Sentinel-1 sensor platforms. The estimation of 100 m resolution wind fields from SAR observations and a geophysical model function (GMF) is provided in Text S1 in Supporting Information S1. Filtering of observations is described in Text S2 in Supporting Information S1, which aims at reducing noise by removing misclassification and images with poor convective signatures.

2.2. Validation

This study uses two validation sources: gridded global reanalysis from ERA5 and point-wise observations from various buoys. Acquisition details for both are described in Text S1 in Supporting Information S1. ERA5 is used in direct comparison with our estimates. Buoy observations are used as a check on ERA5's validity.

Global hourly validation data on single levels at $1° \times 1°$ resolution is downloaded from ECMWF's ERA5 reanalysis data set (Hersbach et al., 2018). Each scene is co-located with the nearest ERA5 grid cell. The ERA5 parameters, along with the latitude and respective measurement heights, are fed into the COARE-like algorithm COARE3.5, available at Ifremer (2015) and based on COARE3 from Fairall et al. (2003), yielding a value of Obukhov length based on ERA5 data only (L_{ERA5}).

The validity of using ERA5 data for validation is assessed in Text S1 in Supporting Information S1. For a small sample of triple co-locations (ERA5, SAR, buoys), buoy and ERA5-retrieved validation were found to be approximately equally representative of the atmosphere as extracted from SAR imagery. A separate analysis between triple co-located buoys and ERA5 confirmed a minimum of 75.9% of the latter's signal is physically based (up to +80% on a larger data set of buoy-ERA5 co-locations). Under the assumption that the obtained results are representative of ERA5's capabilities beyond direct buoy-ERA5 co-locations, this result justifies the use of ERA5 for validation.

3. Methodology

3.1. SAR Spectral-Derived Parameters

High-resolution SAR enables the calculation of high-resolution wind-field spectra. This study utilizes information derived from both the one- and two-dimensional wind-field spectra. Our one-dimensional spectra are similar to Figure 2 in Young et al. (2000), with the important distinction that ours are constructed through polar integration. A polar integration of the two-dimensional spectrum is more robust than the equivalent obtained from a one-dimensional cross section. It prevents high-wavenumber noise (such as from swell) projecting itself onto the relevant, larger scales (see Text S2 in Supporting Information S1). Furthermore, polar integrations negate the need to rotate and clip images along a particular axis. However, as a trade-off this method adds extra sensitivity to noise occurring at the wavelengths of interest, regardless of orientation. Parameters derived from the two-dimensional spectra are related to spectral-energy contours and orientation. These give insight into the spread and directionality of the spectrum. Details on the derived parameters can be found in Text S2 in Supporting Information S1, with an example shown in Figure S1 in Supporting Information S1.

3.2. Analysis Frameworks

3.2.1. Analytical Approach

The analytical approach follows the methodology of Young et al. (2000), which assumes a correlation between the sea-surface roughness patterns detected by SAR and the atmosphere above. Specifically, the magnitude of backscatter relates to the wind-induced shear component whereas the backscatter variations are related to the turbulent eddies of the convective component. Having computed a wind field and its one-dimensional spectrum, corresponding shear and convective components are calculated following Young et al. (2000) in Text S2 in Supporting Information S1. Eight physically related parameters are computed during this stage including the analytical estimate of Obukhov length, $\widehat{L}$.

3.2.2. Machine-Learning Assisted Approach

Machine Learning (ML) is employed in an effort to overcome inadequacies in, and deviations from, the analytical approach. Parameters from the analytical approach are fed into a ML regression algorithm along with additional zero-dimensional parameters retrieved from the one- and two-dimensional spectrum and the SAR viewing geometry, yielding a second estimate of the Obukhov length, $\widehat{L}_{\mathrm{ML}}$. ML is expected to improve upon the initial estimate by learning when to account for systematic biases and errors. Several distinct ML algorithms are trained in this study. Their general design and training process remain the same. Differences between ML algorithms relate only to the data on which they are trained, unless specified otherwise. The data preparation prior to ML, such as filtering, and a description of the regression itself are presented in Text S2 in Supporting Information S1.

4. Results

4.1. SAR Observed MABL Rolls

Analytical and ML results, $\widehat{L}$ and $\widehat{L}_{\mathrm{ML}}$, are presented in the top panel of Figure 2 respectively. Between $10 \leq |L_{\mathrm{ERA5}}| \leq 100$ m the median trendline of $\log_{10}\left(\widehat{L}\right)$ appears to follow the slope of ERA5 validation, though with a bias and significant noise. Beyond $|L_{\mathrm{ERA5}}| = 100$ m the analytical methodology appears incapable of differentiating between stability states. The ML-assisted approach increases both the precision and accuracy of estimates. Additionally, where estimates from the analytical approach plateau, the ML-assisted approach remains capable of discerning between stability states. The ML-assisted method suffers from underestimation for $|L_{\mathrm{ERA5}}| \geq 100$ m and overestimation for $|L_{\mathrm{ERA5}}| \leq 100$ m. This is likely an artifact of the non-uniform distributed data as visible in the histograms of Figure 2.

Quantitative assessments are performed using the coefficient of determination (R^2) and median absolute error (MAE) on logarithmic $|L|$-values. The former gives insight into the average—and therefore outlier-sensitive—performance. The more robust MAE yields insight into the systematic performance. R^2 values can be interpreted as the fraction of explained variance. An antilog of MAE yields the median relative error (MRE) on a non-logarithmic scale. Mean and standard deviations are obtained through a five-fold cross validation.

Analytical results in the upper left panel of Figure 2 do not linearly follow validation data (yielding a negative R^2). When assisted by ML the R^2 metric increases to 0.673 (see Table 1); the ML algorithm can account for over two-thirds of the observed variance. Antilogs of MAE's 0.341 and 0.113 yields MRE's of 119% and 30% for $\widehat{L}$ and $\widehat{L}_{\mathrm{ML}}$ respectively; the MRE error decreases by a factor four when assisted by ML, resulting in half of the ML-assisted estimates experiencing a relative error in L-estimation of less than 30%. Performance varies little across the relevant scales of turbulence, as detailed in Text S3 in Supporting Information S1, such that the methodology can be used for both microscale and mesoscale turbulence. A spatiotemporal analysis of results is provided in Text S3 in Supporting Information S1, from which can be deduced that $\widehat{L}_{\mathrm{ML}}$ estimates are qualitatively similar to L_{ERA5} (unlike $\widehat{L}$) and that coherent correlated errors between the two suggest regional phenomena, such as currents, may induce errors.

Additional ML algorithms are trained on a subset of available parameters to assess their respective prediction importance (see Table 1). When trained on a single parameter, estimated median neutral wind speed $\tilde{U}_n$, the ML algorithm already outperforms the results from the analytical approach and is able to explain 47.6% of the observed L_{ERA5} variance. Including two parameters related to the viewing geometry (radar incidence angle ϕ and spectral energy direction in range δ), for a total of three parameters, increases the explainable variance by
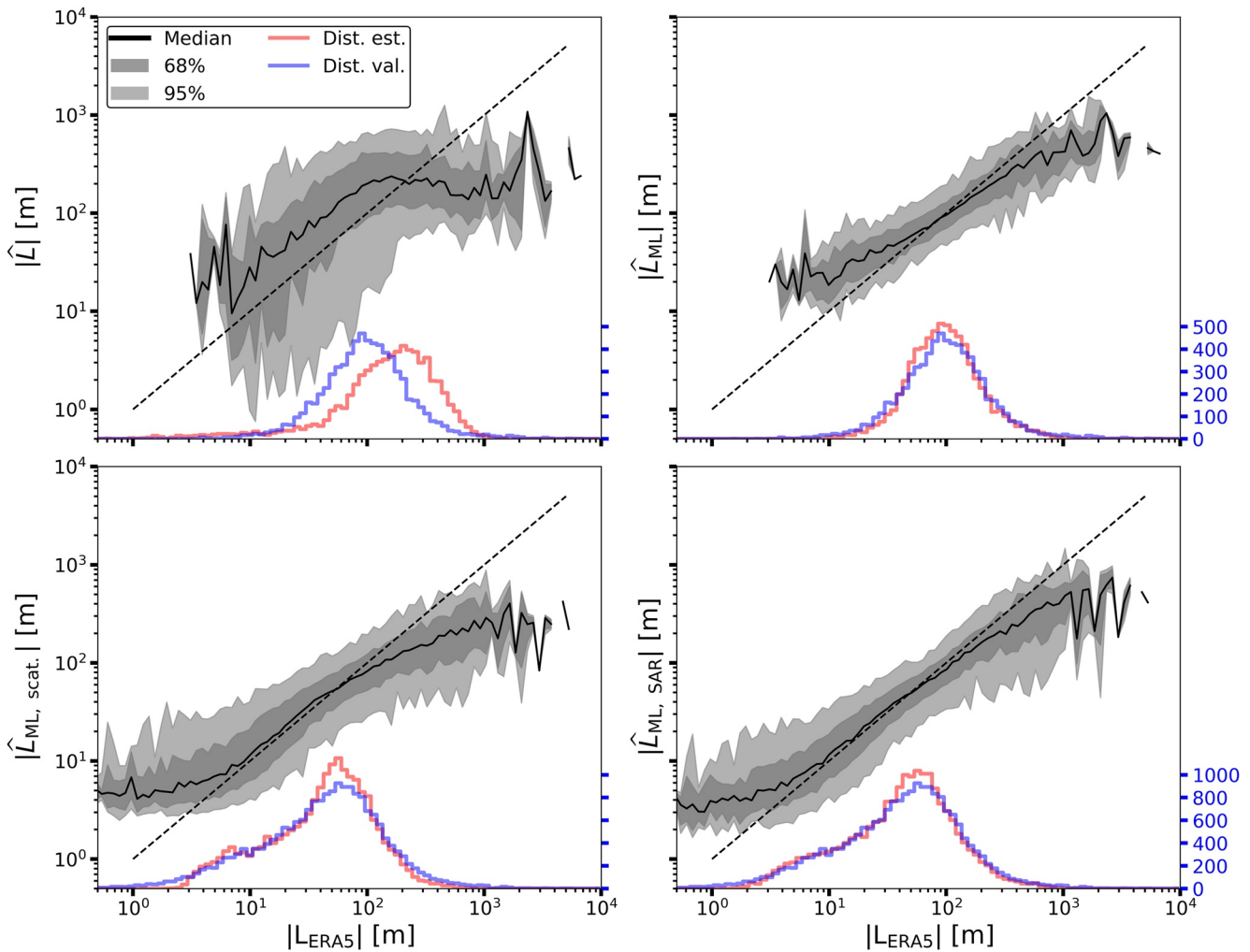
Figure 2. ERA5 validation versus (top left) analytical L estimates on rolls, (top right) ML-assisted L estimates on rolls, (bottom left) ML-assisted L estimates on rolls and cells from synthetic scatterometer, (bottom right) ML-assisted L estimates on rolls and cells. Histograms of estimation and validation values of L included.

nearly 7%-points to 54.4%; the predictive power extracted from three parameters accounts for over 80% of the total predicted variance. The predictive power contained within $\tilde{U}_n$ logically follows from Equation 1, wherein wind speed directly affects the wind-shear component $u*$ and is correlated to $\overline{w'T_v'}$. However, neither viewing geometry parameter is considered in the analytical framework, nor should the atmospheric state depend on them. Yet ϕ and δ experience a Pearson's correlation coefficient of 0.27 and 0.31 with $\log_{10}(|L_{\mathrm{ERA5}}|)$ respectively.

Table 1
Estimation Performance as a Function of Parameters Included in Machine Learning Algorithms

# Params		1	3	9	35	43
$\hat{L}_{\mathrm{ML}}$	R^2	0.476 ± 0.019	0.544 ± 0.011	0.529 ± 0.023	0.651 ± 0.013	0.673 ± 0.015
	MAE	0.158 ± 0.004	0.144 ± 0.003	0.149 ± 0.003	0.117 ± 0.002	0.113 ± 0.001
$\hat{L}_{\mathrm{ML,R\&C}}$	R^2	–	0.709 ± 0.004	–	–	0.796 ± 0.005
	MAE	–	0.161 ± 0.004	–	–	0.125 ± 0.003

Note. First the ML algorithm is trained on a single parameter, $\tilde{U}_n$. Next parameters ϕ and δ are included, for a total of three parameters. Then the analysis is performed on $\tilde{U}_n$ in addition to eight parameters uniquely calculated in the analytical approach (e.g., $\log_{10}\left(|\hat{L}|\right)$, $u*$, z_0, C_{dn}, σ_u, B, w_*, and χ) for a total of nine parameters. Afterward all spectral-derived parameters (with the exception of the previous eight) are considered in addition to $\tilde{U}_n$, ϕ and δ for a total of 35 parameters. Lastly, the ML algorithm is trained on all 43 parameters. The R&C results are obtained from a ML algorithm trained on a larger data set comprising both rolls and cells.

This indicates a sampling bias introduced by the classification algorithm of Wang, Tandeo, et al. ([2019](#)) with specific atmospheric conditions being more frequently detected during specific viewing geometries, for example, low values for $|L_{\mathrm{ERA5}}|$ are disproportionately sampled at smaller incidence angles (WV1) with wind directions propagating in the along-range direction. Vice versa for greater $|L_{\mathrm{ERA5}}|$ values. A more detailed analysis on the influence of δ on estimation performance is included in Text S3 in Supporting Information [S1](#), whose results suggest a decrease in atmospheric information captured in SAR imagery as a function of δ. Combining $\tilde{U}_n$ with eight parameters derived uniquely in the analytical approach (for a total of nine) yields poorer performance than the model trained on three parameters; parameters retrieved from the analytical approach appear to contain little predictive power beyond that already contained in the wind-speed estimate. The ML algorithm trained on all parameters but those retrieved from the analytical approach, for a total of 35 parameters, explains 65.1% of variance. Lastly, when including the eight previously omitted parameters, for a total of 43 parameters, 67.3% of variance is explained. Therefore, the parameters from the analytical approach uniquely contribute 2.2%-points. A more detailed variance budget is provided in Text S3 in Supporting Information [S1](#), which also includes the validation data components.

4.2. SAR Observed MABL Rolls and Cells

We perform new analyses on scenes classified as cells in addition to rolls to extend the model for a broader range of convective conditions and to determine whether wind speed remains the dominant predictor across classes. A new ML algorithm is trained on composite data containing the original rolls and approximately twice as many cells (R&C). Data set details are provided in Text S2 in Supporting Information [S1](#).

Estimation results of the new ML algorithm, $\hat{L}_{\mathrm{ML,R\&C}}$, are shown in the bottom right panel of Figure [2](#). Qualitatively, the $\hat{L}_{\mathrm{ML,R\&C}}$ estimates appear as an extension toward greater instabilities from $\hat{L}_{\mathrm{ML}}$. The greater spread in the distribution of L_{ERA5} corresponding to $\hat{L}_{\mathrm{ML,R\&C}}$ allows the new ML algorithm to remain unbiased for a greater range between approximately $10 \leq |L_{\mathrm{ERA5}}| \leq 100$ m. An apparent asymptote at $|L_{\mathrm{ERA5}}| \leq 10$ m prevents correct estimation for very unstable scenes. This may be the result of fewer observations nearing said asymptote, or due to the fleeting nature of very unstable atmospheric conditions causing greater decorrelation between observation and validation. The R^2 metric for $\hat{L}_{\mathrm{ML,R\&C}}$ shoots up to 0.795 as compared to 0.673 from $\hat{L}_{\mathrm{ML}}$, indicating that L-estimation can successfully be applied on a broad range of stabilities. The near three-fold increase in observations is likely to account for part of the apparent improvement, as is the increased spread of L_{ERA5}: the R^2 metric weights errors inversely proportional to the variance of the validation data, which is greater when considering both cells and rolls. Meanwhile the MAE metric of $\hat{L}_{\mathrm{ML,R\&C}}$ increases slightly to 0.125 as compared to 0.113 from $\hat{L}_{\mathrm{ML}}$; despite significantly increasing the range of estimation possibilities, the median error only marginally increases.

5. Discussion

Roll-analysis results indicate that two-thirds of the predictive power is extracted from the GMF-retrieved median wind speed. A second analysis on both rolls and cells indicates an even greater relative importance of wind speed on stability estimations. These observations may give the impression of high-resolution information being redundant. The additional value of high-resolution SAR observations is perhaps best illustrated by an example. The two SAR scenes in Figure [1](#) occurred during similar wind speeds and are part of the test fraction of data. They are classified as containing rolls and cells respectively, with ERA5 confirming that the right-hand figure occurred in a more unstable regime. Predictions from the ML algorithm trained on parameters derivable through SAR ($\hat{L}_{\mathrm{ML,R\&C}}$ trained on all available 43 parameters), L_{SAR}, are significantly closer to validation than L_{scat} ($\hat{L}_{\mathrm{ML,R\&C}}$ trained only on parameters obtainable from hypothetical scatterometers, i.e., $\tilde{U}_n$, ϕ and δ). Since $\tilde{U}_n$'s are similar and both observations were made at the same incidence angle, the only remaining degree of freedom is δ, whose prediction contribution springs from observational biases. Therefore, the contribution of parameters obtainable with high-resolution SAR appears to mainly lie in error reduction rather than first-order approximations. This finding also holds on a statistical level as is evident from the results in Table [1](#) demonstrating that high-resolution related parameters result in a relatively greater decrease in MAE than the relative increase R^2.

Globally L_{SAR} consistently outperforms L_{scat} in our preliminary investigation. Therefore, by mapping the differences between the two we can identify where the ML algorithm benefits from high-resolution information (see

Figure 3. Global difference between L_{SAR} and L_{scat} on $2.5° \times 2.5°$ for the 20% test fraction of the composite data set.

Figure 3). Regionally coherent structures, such as off the North American East Coast, suggest local importance of high-resolution information. In the past, this region was the subject of studies investigating current signatures of the Gulf Stream in SAR imagery (e.g., Beal et al., 1997; Marmorino et al., 1997). The Gulf Stream's warm currents transport heat from the tropics up to the mid-latitudes, where the resulting enhanced air-sea temperature gradient provides ample opportunity for atmospheric convection. Even more so when the prevailing westerlies transport cold continental air over the warmer western boundary current. The negative sign of the structure indicates $|L_{scat}|$ underestimates the atmospheric instability with respect to $|L_{SAR}|$ (and $|L_{ERA5}|$); without kilometer-scale texture information L_{scat} is incapable of estimating atmospheric instability beyond a first-order approximation. Consequently, we deduce from this regional example, the comparison discussed in Figure 1 and the summary statistics in Table 1 that kilometer-scale texture information is needed to uniquely distinguish between instabilities. Furthermore, kilometer-scale information is prerequisite on account of having to identify convective SAR scenes.

Naturally results would change as a function of data distribution. If our data set had contained excessive observations over the Gulf Stream, estimation for this region would improve (regardless of parameters included) at the expense of all other regions. Similarly, estimation will be poor for any new observation with previously unsampled convective signatures. The presented performance should therefore be seen as secondary to the facts that L can quantitatively be extracted from SAR scenes and that robust extraction necessitates high-resolution information. Without this information and following Equation 1, L-estimates would provide poor constraints on momentum and heat fluxes—in particular for infrequently sampled regions with unique convection-driving mechanisms—across the air-sea interface. This could subsequently affect derived regional weather forecasts and, potentially, cascade into erroneous climatological predictions.

6. Conclusion and Perspective

Results confirm the possibility of inferring stability conditions at the air-sea interface from SAR imagery. The analytical method proposed by Young et al. (2000) has limited applicability but provides useful guidance and parameters with which to filter non-convective observations. Our method, based on a ML algorithm trained on zero-dimensional parameters, demonstrates a leap forward in performance. The MAE largely drops while R^2 increases, suggesting that 67.3% of the validation variance can be explained for rolls, and up to 79.6% when considering rolls and cells. Accordingly, atmospheric information can be extracted from relatively simple parameters to discriminate between an already narrow range of atmospheric states.

Much of the prediction power could be achieved with scatterometer measurements due to the importance of wind speed in making a first-order approximation. Though, texture-related parameters derived from high-resolution SAR scenes enable a significant reduction in errors. In fact, without information on kilometer-scale features, the ML algorithm is incapable of providing more than a first-order approximation.

Future high-resolution Earth observation missions, such as EE10 Harmony (ESA, 2022) and the proposed EE11 SEASTAR (Gommenginger et al., 2019), could improve results by providing multiple observations obtained from additional viewing angles. With the added degrees of freedom, it may be possible to identify, learn and infer what

atmospheric information might else be lost as a function of viewing geometry. In turn, this would allow for the creation of a global convective-scenes data set unbiased by viewing geometry.

The presented results illustrate the prediction potential when trained exclusively on a parameterized model. A new generation of co-located validation data is needed to go beyond the current ML predictions, to make estimates independent of and surpassing ERA5. However, the present predictions can already be employed to improve parameterization despite being trained toward a parameterized model. Discrepancies between our estimates and ERA5 may highlight where the latter falls short (e.g., poorly parameterized regions/phenomena). Future work could include localized ground truth measurements, regional models and ancillary information into the training data to locally enhance predictions. A ML model trained on such enhanced databases could in turn provide new constraints on parameterized models by providing vast quantities of estimates covering complex phenomena. After all, Sentinel-1 satellites promise decades of data and continuity.

Additionally, enhanced wind-field inversion schemes would evidently benefit from including high-resolution texture information to retrieve non-neutral wind-fields and stability information (as opposed to the scatterometer-based statistical inversion schemes in CMOD5). If incorporated in a deterministic manner, an improved understanding of the connection between textures and stability conditions would be required. This connection may be inferred from the ML algorithm itself by deliberate manipulation of the testing data set (and study of its propagated effect), by dissecting the ML algorithm itself (akin to studying the intermediate layers of a neural network) or through joint analysis of wide-swath predictions with corresponding large eddy simulations. Furthermore, the ML algorithm could be applied and/or trained on LES-retrieved wind fields to aid in constraining new inversion schemes developed on LES-derived backscatter fields.

Lastly, our methodology could serve as an example to future studies on leveraging preexisting databases of satellite observations in combination with ML for preliminary feasibility assessment. Future studies can go beyond Obukhov length and employ the same methodology on other/additional data sets to estimate parameters related to the Richardson number, ocean currents and heat fluxes.

Data Availability Statement

This study relied on buoy measurements, ERA5 reanalysis and Sentinel-1 acquisitions. Processed data is available at https://doi.org/10.5281/zenodo.7801577. A GitHub repository with example notebooks is provided at github. com/owenodriscoll/supplement_paper and https://doi.org/10.5281/zenodo.8064027. Raw data for the WHOTS and Stratus buoys are available at WHOI (2022). Additional buoys off the North American coast are made available by NOAA at NDBC (2022), with data from the PAPA network available at NOAA (2022b) and data from the Triton, RAMA and PIRATA buoy networks available at NOAA (2022a). ERA5 data (Hersbach et al., 2018) is made available by the Copernicus Climate Change Service at https://doi.org/10.24381/cds.adbb2d47. The Sentinel-1 SAR images are hosted by Ifremer, whose data set contains Copernicus Sentinel data (2022). Freely accessible Sentinel-1 data is available at ESA's Sentinel Open Access Hub https://sentinel.esa.int/web/sentinel/sentinel-data-access.

References

Alpers, W., & Brümmer, B. (1994). Atmospheric boundary layer rolls observed by the synthetic aperture radar aboard the ERS-1 satellite. *Journal of Geophysical Research*, *99*(C6), 12613–12621. https://doi.org/10.1029/94jc00421

Beal, R., Kudryavtsev, V., Thompson, D., Grodsky, S., Tilley, D., Dulov, V., & Graber, H. (1997). The influence of the marine atmospheric boundary layer on ERS 1 synthetic aperture radar imagery of the Gulf Stream. *Journal of Geophysical Research*, *102*(C3), 5799–5814. https://doi.org/10.1029/96jc03109

Bony, S., Stevens, B., Ament, F., Bigorre, S., Chazette, P., Crewell, S., et al. (2017). EUREC 4A: A field campaign to elucidate the couplings between clouds, convection and circulation. *Surveys in Geophysics*, *38*(6), 1529–1568. https://doi.org/10.1007/s10712-017-9428-0

Brüning, C., Alpers, W., & Hasselmann, K. (1990). Monte-Carlo simulation studies of the nonlinear imaging of a two dimensional surface wave field by a synthetic aperture radar. *International Journal of Remote Sensing*, *2*(10), 1695–1727. https://doi.org/10.1080/01431169008955125

Christensen, H., & Zanna, L. (2022). Parametrization in weather and climate models. In *Oxford research encyclopedia of climate science*.

Copernicus Sentinel Data (2022). Retrieved from ifremer, processed by esa. Ifremer. (Years of data acquisition: 2020 and 2021. Available at https://sci-hub.copernicus.eu/

Cronin, M. F., Gentemann, C. L., Edson, J., Ueki, I., Bourassa, M., Brown, S., et al. (2019). Air-sea fluxes with a focus on heat and momentum. *Frontiers in Marine Science*, *6*, 430. https://doi.org/10.3389/fmars.2019.00430

ESA. (2021). Sentinel-1 SAR instrument. Retrieved from https://sentinel.esa.int/web/sentinel/technical-guides/sentinel-1-sar/sar-instrument

ESA. (2022). Report for mission selection: Earth explorer 10 candidate mission harmony (Tech. Rep.).

Fairall, C. W., Bradley, E. F., Hare, J., Grachev, A. A., & Edson, J. B. (2003). Bulk parameterization of air–sea fluxes: Updates and verification for the coarse algorithm. *Journal of Climate*, *16*(4), 571–591. https://doi.org/10.1175/1520-0442(2003)016<0571:bpoasf>2.0.co;2

Fiedler, F., & Panofsky, H. A. (1970). Atmospheric scales and spectral gaps. *Bulletin of the American Meteorological Society*, *51*(12), 1114–1120. https://doi.org/10.1175/1520-0477(1970)051<1114:asasg>2.0.co;2

Gommenginger, C., Chapron, B., Hogg, A., Buckingham, C., Fox-Kemper, B., Eriksson, L., et al. (2019). Seastar: A mission to study ocean submesoscale dynamics and small-scale atmosphere-ocean processes in coastal, shelf and polar seas. *Frontiers in Marine Science*, *6*, 457. https://doi.org/10.3389/fmars.2019.00457

Grossman, R. L. (1982). An analysis of vertical velocity spectra obtained in the bomex fair-weather, trade-wind boundary layer. *Boundary-Layer Meteorology*, *23*(3), 323–357. https://doi.org/10.1007/bf00121120

Hersbach, H., Bell, B., Berrisford, P., Biavati, G., Horányi, A., Muñoz Sabater, J., et al. (2018). ERA5 hourly data on single levels from 1959 to present. [Dataset]. Copernicus Climate Change Service (C3S) Climate Data Store (CDS). https://doi.org/10.24381/cds.adbb2d47

Ifremer (2015). Cerform scientific modules [Software]. https://cerform.readthedocs.io/en/latest/api/cerform.flux.html#module-cerform.flux.coare4

IPCC. (2013). In *Climate Change 2013: The Physical Science Basis. Contribution of Working Group I to the Fifth Assessment Report of the Intergovernmental Panel on Climate Change*, (pp. 255–316). Cambridge University Press. https://doi.org/10.1017/CBO9781107415324.010

Kaimal, J., Wyngaard, J., Haugen, D., Coté, O., Izumi, Y., Caughey, S., & Readings, C. (1976). Turbulence structure in the convective boundary layer. *Journal of the Atmospheric Sciences*, *33*(11), 2152–2169. https://doi.org/10.1175/1520-0469(1976)033<2152:tsitcb>2.0.co;2

Kaimal, J. C., Wyngaard, J., Izumi, Y., & Coté, O. (1972). Spectral characteristics of surface-layer turbulence. *Quarterly Journal of the Royal Meteorological Society*, *98*(417), 563–589. https://doi.org/10.1002/qj.49709841707

Kerbaol, V., Chapron, B., & Vachon, P. W. (1998). Analysis of ERS-1/2 synthetic aperture radar wave mode imagettes. *Journal of Geophysical Research*, *103*(C4), 7833–7846. https://doi.org/10.1029/97jc01579

Lilly, D. K. (1989). Two-dimensional turbulence generated by energy sources at two scales. *Journal of the Atmospheric Sciences*, *46*(13), 2026–2030. https://doi.org/10.1175/1520-0469(1989)046<2026:tdtgbe>2.0.co;2

Marmorino, G., Thompson, D., Graber, H., & Trump, C. (1997). Correlation of oceanographic signatures appearing in synthetic aperture radar and interferometric synthetic aperture radar imagery with in situ measurements. *Journal of Geophysical Research*, *102*(C8), 18723–18736. https://doi.org/10.1029/97jc01450

Monin, A. S., & Obukhov, A. M. (1954). Basic laws of turbulent mixing in the surface layer of the atmosphere. *Contrib. Geophys. Inst. Acad. Sci. USSR*, *151*(163), e187.

National Academies of Sciences, Engineering, and Medicine. (2019). *Thriving on our changing planet: A decadal strategy for earth observation from space*. National Academies Press. https://doi.org/10.17226/24938

NDBC. (2022). Data source NDBC and TAO buoy network [Dataset]. Retrieved from https://www.ndbc.noaa.gov//obs.shtml

NOAA. (2022a). Data source PAPA buoy network [Dataset]. Retrieved from https://www.pmel.noaa.gov/ocs/data-links

NOAA. (2022b). Data source for TRITON, RAMA and PIRATA buoy networks made available by IFREMER. [Dataset]. Retrieved from http://tds0.ifremer.fr/thredds/catalog/CORIOLIS-OCEANSITES-GDAC-OBS/DATA/catalog.html

Rio, C., Del Genio, A. D., & Hourdin, F. (2019). Ongoing breakthroughs in convective parameterization. *Current Climate Change Reports*, *5*(2), 95–111. https://doi.org/10.1007/s40641-019-00127-w

Rizaev, I., Karakuş, O., Hogan, S. J., & Achim, A. (2021). Modeling and SAR imaging of the sea surface: A review of the state-of-the-art with simulations. arXiv preprint arXiv:2102.05199.

Sikora, T., Young, G., Beal, R., & Edson, J. (1995). Use of spaceborne synthetic aperture radar imagery of the sea surface in detecting the presence and structure of the convective marine atmospheric boundary layer. *Monthly Weather Review*, *123*(12), 3623–3632. https://doi.org/10.1175/1520-0493(1995)123<3623:uossar>2.0.co;2

Sikora, T. D., & Thompson, D. R. (2002). Air-sea turbulence statistics from synthetic aperture radar: An update. *Canadian Journal of Remote Sensing*, *28*(3), 517–523. https://doi.org/10.5589/m02-037

Sikora, T. D., Thompson, D. R., & Bleidorn, J. C. (2000). Testing the diagnosis of marine atmospheric boundary-layer structure from synthetic aperture radar. *Johns Hopkins APL Technical Digest*, *21*(1), 95.

Sikora, T. D., & Ufermann, S. (2004). Marine atmospheric boundary layer cellular convection and longitudinal roll vortices. *Synthetic aperture radar marine user's manual*, 321–330.

Stopa, J. E., Wang, C., Vandemark, D., Foster, R., Mouche, A., & Chapron, B. (2022). Automated global classification of surface layer stratification using high-resolution sea surface roughness measurements by satellite synthetic aperture radar. *Geophysical Research Letters*, *49*(12), e2022GL098686. https://doi.org/10.1029/2022gl098686

Stull, R. B. (1988). *An introduction to boundary layer meteorology* (Vol. 13). Springer Science and Business Media

Vandemark, D., Mourad, P., Bailey, S., Crawford, T., Vogel, C., Sun, J., & Chapron, B. (2001). Measured changes in ocean surface roughness due to atmospheric boundary layer rolls. *Journal of Geophysical Research*, *106*(C3), 4639–4654. https://doi.org/10.1029/1999jc000051

Wang, C., Mouche, A., Foster, R. C., Vandemark, D., Stopa, J. E., Tandeo, P., et al. (2019). Characteristics of marine atmospheric boundary layer roll vortices from Sentinel-1 SAR wave mode. In *IGARSS 2019-2019 IEEE International Geoscience and Remote Sensing Symposium* (pp. 7908–7911).

Wang, C., Mouche, A., Tandeo, P., Stopa, J. E., Longépé, N., Erhard, G., et al. (2019). A labelled ocean SAR imagery dataset of ten geophysical phenomena from sentinel-1 wave mode. *Geoscience Data Journal*, *6*(2), 105–115. https://doi.org/10.1002/gdj3.73

Wang, C., Tandeo, P., Mouche, A., Stopa, J. E., Gressani, V., Longépé, N., et al. (2019). Classification of the global sentinel-1 SAR vignettes for ocean surface process studies. *Remote Sensing of Environment*, *234*, 111457. https://doi.org/10.1016/j.rse.2019.111457

Wang, C., Vandemark, D., Mouche, A., Chapron, B., Li, H., & Foster, R. C. (2020). An assessment of marine atmospheric boundary layer roll detection using sentinel-1 SAR data. *Remote Sensing of Environment*, *250*, 112031. https://doi.org/10.1016/j.rse.2020.112031

WHOI. (2022). Data source Stratus and WHOTS buoy networks of the Woods Hole oceanographic Institution [Dataset]. Retrieved from http://uop.whoi.edu/projects/

Young, G. S., Sikora, T. D., & Winstead, N. S. (2000). Inferring marine atmospheric boundary layer properties from spectral characteristics of satellite-borne SAR imagery. *Monthly Weather Review*, *128*(5), 1506–1520. https://doi.org/10.1175/1520-0493(2000)128<1506:imablp>2.0.co;2

References From the Supporting Information

Akiba, T., Sano, S., Yanase, T., Ohta, T., & Koyama, M. (2019). Optuna: A next-generation hyperparameter optimization framework [Software]. https://doi.org/10.48550/arXiv.1907.10902

Andreas, E. L. (1989). Thermal and size evolution of sea spray droplets.

Bergstra, J., Bardenet, R., Bengio, Y., & Kégl, B. (2011). Algorithms for hyper-parameter optimization, *24*. [Software]. https://dl.acm.org/doi/10.5555/2986459.2986743

Chen, T., & Guestrin, C. (2016). Xgboost: A scalable tree boosting system [Software]. https://doi.org/10.1145/2939672.2939785

Fairall, C. W., Bradley, E. F., Rogers, D. P., Edson, J. B., & Young, G. S. (1996). Bulk parameterization of air-sea fluxes for tropical ocean-global atmosphere coupled-ocean atmosphere response experiment. *Journal of Geophysical Research*, *101*(C2), 3747–3764. https://doi.org/10.1029/95jc03205

Foken, T. (2006). 50 years of the Monin–Obukhov similarity theory. *Boundary-Layer Meteorology*, *119*(3), 431–447. https://doi.org/10.1007/s10546-006-9048-6

Hersbach, H. (2008). *CMOD5.N: A C-band geophysical model function for equivalent neutral wind*. European Centre for Medium-Range Weather Forecasts.

Hersbach, H. (2011). Sea surface roughness and drag coefficient as functions of neutral wind speed. *Journal of Physical Oceanography*, *41*(1), 247–251. https://doi.org/10.1175/2010jpo4567.1

Ke, G., Meng, Q., Finley, T., Wang, T., Chen, W., Ma, W., et al. (2017). Lightgbm: A highly efficient gradient boosting decision tree, *30*. [Software]. https://doi.org/10.5555/3294996.3295074

Li, L., Jamieson, K., DeSalvo, G., Rostamizadeh, A., & Talwalkar, A. (2017). Hyperband: A novel bandit-based approach to hyperparameter optimization. *The Journal of Machine Learning Research*, *18*.

Pedregosa, F., Varoquaux, G., Gramfort, A., Michel, V., Thirion, B., Grisel, O., et al. (2011). Scikit-learn: Machine learning in Python, *12*. [Software]. https://doi.org/10.48550/arXiv.1201.0490

Prokhorenkova, L., Gusev, G., Vorobev, A., Dorogush, A. V., & Gulin, A. (2018). Catboost: Unbiased boosting with categorical features, *31*. [Software]. https://doi.org/10.48550/arXiv.1706.09516

Smith, S. D., Fairall, C. W., Geernaert, G. L., & Hasse, L. (1996). Air-sea fluxes: 25 years of progress. *Boundary-Layer Meteorology*, *78*(3), 247–290. https://doi.org/10.1007/bf00120938